Journal of Hazardous Materials 400 (2020) 123247

Contents lists available at ScienceDirect

Journal of Hazardous Materials

journal homepage: www.elsevier.com/locate/jhazmat

Oil industry waste based non-magnetic and magnetic hydrochar to sequester potentially toxic post-transition metal ions from water

Moonis Ali Khan[a,*], Ayoub Abdullah Alqadami[a], Saikh Mohammad Wabaidur[a], Masoom Raza Siddiqui[a], Byong-Hun Jeon[b], Shareefa Ahmed Alshareef[a], Zeid A. Alothman[a], Abdelrazig Elfaki Hamedelniel[a]

[a] Chemistry Department, College of Science, King Saud University, Riyadh 11451, Saudi Arabia
[b] Department of Earth Resources and Environmental Engineering, Hanyang University, 222, Wangsimni-ro, Seongdong-gu, Seoul, 04763, Republic of Korea

GRAPHICAL ABSTRACT

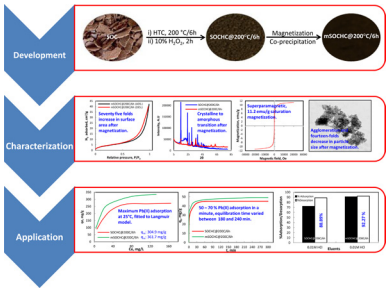

ARTICLE INFO

Editor: L. Eder

Keywords:
Sesame oil cake
Hydrothermal carbonization
Adsorption
Lead
Water treatment

ABSTRACT

Solid waste conversion to value-added products is a stepping stone towards sustainable environment. Herein, sesame oil cake (SOC), an oil industry waste was utilized as a precursor to develop hydrochar (HC) samples by varying reaction temperature (150–250 °C) and time span (2–8 h), chemically treated with 10% H_2O_2 to optimize a sample with maximum yield and Pb(II) adsorption. Highest yield (29.2 %) and Pb(II) (24.57 mg/g at C_o: 15 mg/L) adsorption was observed on SOCHC@200 °C/6 h, magnetized (mSOCHC@200 °C/6 h) for comparative study. XRD displayed highly crystalline SOCHC@200 °C/6 h and amorphous mSOCHC@200 °C/6 h, both having a characteristic cellulose peak at 14.9°. mSOCHC@200 °C/6 h displayed superparamagnetic behavior with 11.2 emu/g saturation magnetization. IR spectra confirmed the development of samples rich in oxygen containing functionalities; an additional peak for iron oxides appeared at 586 cm^{-1} in mSOCHC@200°C/6 h spectrum. Four major peaks at 531.9, 399.9, 348.2 and 284.7 eV, assigned to O 1s, N 1s, Ca 2p and C 1s, respectively were observed during XPS analyses. An additional peak at 710.3 eV, ascribed to Fe 2p was observed in mSOCHC@200C/6 h XPS spectrum, while a peak at 143.2 eV for Pb 4f appeared in spectra of both Pb(II) saturated samples. pH dependent (maximum at ~6.7), exothermic Pb(II) adsorption was found. About 50–70% (at C_o: 25 mg/L) adsorption on both SOCHC@200 °C/6 h and mSOCHC@200 °C/6 h was accomplished in a minute, attaining equilibrium in 180 and 240 min, respectively. Error functions and superimposed $q_{e,\ exp.}$ and $q_{e,\ cal.}$ values supported Langmuir isotherm model applicability, with respective q_m values of 304.9 and 361.7 mg/g at 25 °C for SOCHC@200 °C/6 h and mSOCHC@200 °C/6 h. Kinetic data was fitted to PSO model. Highest (between 92.2 and 88.9 %) amount of Pb(II) from SOCHC@200 °C/6 h and mSOCHC@200 °C/6 h was eluted by 0.01 M HCl.

* Corresponding author.
E-mail address: mokhan@ksu.edu.sa (M.A. Khan).

https://doi.org/10.1016/j.jhazmat.2020.123247
Received 12 May 2020; Received in revised form 15 June 2020; Accepted 16 June 2020
Available online 19 June 2020

1. Introduction

Comparatively shorter reaction span, minimal energy consumption, and production of solid carbon-rich fuel along with value-added liquid products had established hydrothermal carbonization (HTC) as a prominent pyrolysis technique. Besides, HTC can convert wet biomass into hydrochar (HC) while avoiding energy intense biomass drying step. Therefore, the process can also be alternately term as wet pyrolysis. During HTC reaction, the precursor material (suspended in subcritical water) under goes thermo-chemical reaction steps including hydrolysis of the extractives, followed by dehydration and thereafter decarboxylation, condensation, polymerization, and aromatization in liquid phase (Fernandez et al., 2015). These steps results in development of carbonaceous product (HC) with hydrophobic core and hydrophilic shell (Kazak and Tor, 2020). Generally, HC exhibits higher heating values which displayed its energy source potentiality. Moreover, the presence surface functionalities (specifically oxygen containing functionalities, such as C = O, C–O, and O–H (Hu et al., 2020)) and higher cation exchange capacity (CEC) uncovered its potential usage as a storage material, a catalyst, and an adsorbent (Román et al., 2013), while the hydrophilic characteristic of HC could be utilized to increase soil's water retention potential (Kambo and Dutta, 2015).

Development of HC from sewage, municipal, industrial and agro-wastes from HTC technique for environmental applications is well reported (Spataru et al., 2016; Oliver-Tomas et al., 2019; Teng et al., 2020; Tran et al., 2020). Oil cake/meal, an agro-waste, generated after the extraction of oil from the edible and non-edible seeds. Edible oil cakes are rich in proteins, could be used as animal feed. On the other hand, non-edible oil cakes have higher nitrogen, phosphorous, and potassium content, could be utilized as green manure for plants growth. Researchers have reported the use of oil cakes in aqueous environment decontamination. Soya oil cake was utilized to adsorb and reduce Cr (VI) from water (Daneshvar et al., 2002). The adsorption of Zr(IV) on karanja oil cake at initial concentration (C_o): ~75 mg/L and pH: 3.6 was 23.4 mg/g (Varala et al., 2016). Batch and column mode experiments were carried out to test the adsorption efficacy of pongamia oil cake based adsorbent for Zn(II) removal from water, while maximum Zn(II) recovery was observed with 0.1 M EDTA (Shanmugaprakash and Sivakumar, 2015). The adsorption of Cu(II) was studied on mustard oil cake with 0.717 mmol/g as a maximum uptake capacity (Ajmal et al., 2005). Single and multi-metal systems adsorption of Cu(II), Pb(II), and Cd(II) by both batch and column scale experiments on neem oil cake was reported (Rao and Khan, 2007). Konstantinou and co-workers have studied the adsorption of Cu(II) and Eu(III) on olive oil cake (Konstantinou et al., 2007). Also, there are studies reporting the thermal and chemical modifications of oil cakes and their applications in environmental remediation. Castor oil cake was pyrolyzed to biochar at 500–900 °C, chemically activated with K_2CO_3 and tested in the removal of methylene blue (MB) with 99.6 % removal efficiency (Sánchez-Cantú et al., 2018). Carbon-based microporous adsorbent with high surface area was developed from rape oil cake at 800 °C, chemically activated with Na_2CO_3, and utilized for the removal of bivalent Pb(II) and Ni(II) ions from water (Uçar et al., 2015). Activated carbon derived from sunflower oil cake was chemically modified with H_2SO_4 to sequester MB from water with 16.4 mg/g as maximum uptake capacity (Karagöz et al., 2008).

Sesame or gingelly (*Sesamum indicum* L.) is an edible oil crop of Pedaliaceae family, found in tropical and subtropical areas of Asia, Africa, and South America, has high degree of resistance to oxidation and rancidity (Bedigian and Harlan, 1986). Compositional analysis of sesame oil cake (SOC) showed the presence of significantly high (35.6 %) crude protein content along with crude fiber (7.6 %), calcium (2.5 %), and phosphorous (1.1 %) (Kuo, 1967), which makes it a cost-effective animal feed. Besides, better nutritional value favors it usage as a green manure. Studies have reported the environmental remediation applications of SOC. It was utilized in the removal of Cu(II) from water with 4.24 mg/g removal efficiency at pH: 5, T: 40 °C, and C_o: 10 mg/L (Kumar et al., 2019). Char was developed from SOC, chemically activated by $H_2SO_4/ZnCl_2$ and tested in Cr(VI) removal (Nagashanmugam, 2018). Activated carbon derived from SOC was tested in Pb(II) removal with 105.3 mg/g uptake capacity (Nagashanmugam and Srinivasan, 2010). Based on our knowledge upon comprehensive literature survey, to-date, studies are rear on development of HC from SOC. Thus, present study proposed the development of HC from SOC (SOCHC). Developmental conditions were optimized by varying HTC reaction temperature (150–250 °C), and time span (2–8 h). Further, SOCHC samples were chemically treated with 10 % H_2O_2 solution. A sample with maximum HC yield (%) and lead [Pb(II)] removal efficiency from water was selected for detailed adsorption studies. Additionally, to ease up phase separation process the optimized sample was magnetized (mSOCHC) by co-precipitation methodology. Both non-magnetic and magnetic samples were characterized and adsorption/desorption of Pb (II) through batch mode experiments was comprehensively studied.

Table 1
Developmental conditions, functionalities concentration, and Pb(II) uptake over SOCHC samples.

Sample	Developmental conditions			Yield (%)	Functionalities concentration(FC)		Pb(II) uptake	
	Physical		Chemical		Base(BFC, meq./g)	Acid(AFC, meq./g)	Adsorption (%)	Adsorption capacity (q_e, mg/g)
	Temp. (T, °C)	Time (t, h)						
S1	150	2	10 % H_2O_2	52	0.745	1.030	70.1	18.98
S2	150	4	10 % H_2O_2	39	0.730	1.040	85.2	20.10
S3	150	6	10 % H_2O_2	36	0.760	1.070	83.8	18.29
S4	150	8	10 % H_2O_2	31	0.770	1.100	89.8	18.84
S5	200	2	10 % H_2O_2	34	0.700	1.060	80.7	18.39
S6	200	4	10 % H_2O_2	28	0.720	1.160	96.7	22.01
S7	200	6	10 % H_2O_2	29.2	0.740	1.020	97.2	24.57
S8	200	8	10 % H_2O_2	29	0.740	1.080	97.3	24.89
S9	250	2	10 % H_2O_2	32	0.735	1.555	92.0	21.44
S10	250	4	10 % H_2O_2	27	0.715	1.060	96.9	24.72
S11	250	6	10 % H_2O_2	28.4	0.765	1.025	96.7	22.37
S12	250	8	10 % H_2O_2	26.5	0.755	1.015	91.6	14.85

2. Experimental

2.1. Chemicals and reagents

The chemicals and reagents used during the study were of analytical reagent (A.R.) grade or as itemized. Stock solution of Pb(II) (1000 mg/L) was prepared from lead nitrate ($Pb(NO_3)_2$, BDH, England) salt. Hydrogen peroxide (H_2O_2, 30 %, Merck, Germany) was used for chemical modification of HC. Ferric chloride hexa hydrate ($FeCl_3.6H_2O$, Sigma-Aldrich, USA), ferrous chloride tetra hydrate ($FeCl_2.4H_2O$, Sigma-Aldrich, USA), ammonium hydroxide (NH_4OH, 25 %, Merck Germany), and ethanol (C_2H_5OH, Fischer Scientific, UK) were used to magnetize HC. Hydrochloric acid (HCl, Merck, Germany), nitric acid (HNO_3, Merck, Germany), sulfuric acid (H_2SO_4, Merck, Germany), and sodium hydroxide (NaOH, BDH, England) were used to adjust pH and during regeneration study. Deionized (D.I.) water from Milli-Q water purification system (Millipore, USA) was utilized during the study.

2.2. Development and magnetization of SOC hydrochar

In a 250 mL graduated beaker, 10 g of SOC (collected from a local oil mill, India) was taken, washed several times with D.I water to remove traces of dirt and dust. Thereafter, 90 mL D.I water was added to SOC for making slurry. The slurry was transferred to 200 cc hydrothermal carbonization (HTC) reactor with polytetrafluroethylene (PTFE) tube lining. The reactor was sealed, heated in an oven at 5 °C/min heating rate, while pressure was autogenous. The heating temperature (150 and 250 °C) and time (2 and 8 h) were varied to optimize a SOC hydrochar (SOCHC) sample (out of twelve developed samples) with maximum Pb(II) removal, along with better yield (Table 1). The developed SOCHC samples were chemically treated for 2 h under magnetic stirring at 100 rpm with 100 mL 10 % H_2O_2, thereafter; samples were washed several times with D.I. water until the pH of rinsing D.I. water was reached near to neutral. The brownish outlook samples were overnight dried at 60 °C, manually crushed to powder with mortar and pestle, and finally sieved to a uniform particle size, thereafter, stored in sealed polyethylene bags for studies. By comparing both developmental conditions and yield, sample S7, with 24.6 mg/g Pb(II) uptake and 29.2 % yield was selected for detailed adsorption studies. Hereafter, sample S7, schematically illustrated in Scheme 1 was nomenclature as "SOCHC@200 °C/6 h".

The SOCHC@200 °C/6 h was magnetized by co-precipitation methodology. In a typical procedure, one gram of SOCHC@200 °C/6 h under continuous mechanical stirring was dispersed in 200 mL D.I. water. Thereafter, under continuous stirring $FeCl_3.6H_2O$ (2.36 g) and $FeCl_2.4H_2O$ (1.18 g) in 2:1 molarM ratio were added to the dispersion. To avoid oxidation of iron salts nitrogen gas was purged into the suspension. The sample was aged for 60 min under continuous mechanical stirring at 100 rpm. Thereafter, ammonium hydroxide solution (25 mL) was added drop-by-drop through a dropper to dispersion under high speed (1000 rpm) mechanical stirring. Further, the stirring continues for 30 min. Finally, a black color precipitate nomenclature as "mSOCHC@200 °C/6 h" and illustrated in Scheme 1 was formed, magnetically separated by external magnetic field, washed with D.I. water to neutral pH, and finally washed with ethanol.

2.3. Characterization

The respective surface morphologies and elemental content of SOCHC@200 °C/6 h and mSOCHC@200 °C/6 h samples were analyzed by high resolution-scanning electron microscopy coupled with energy dispersive X-ray analysis (HRSEM-EDX, LV-SEM; S-3500 N, Hitachi at

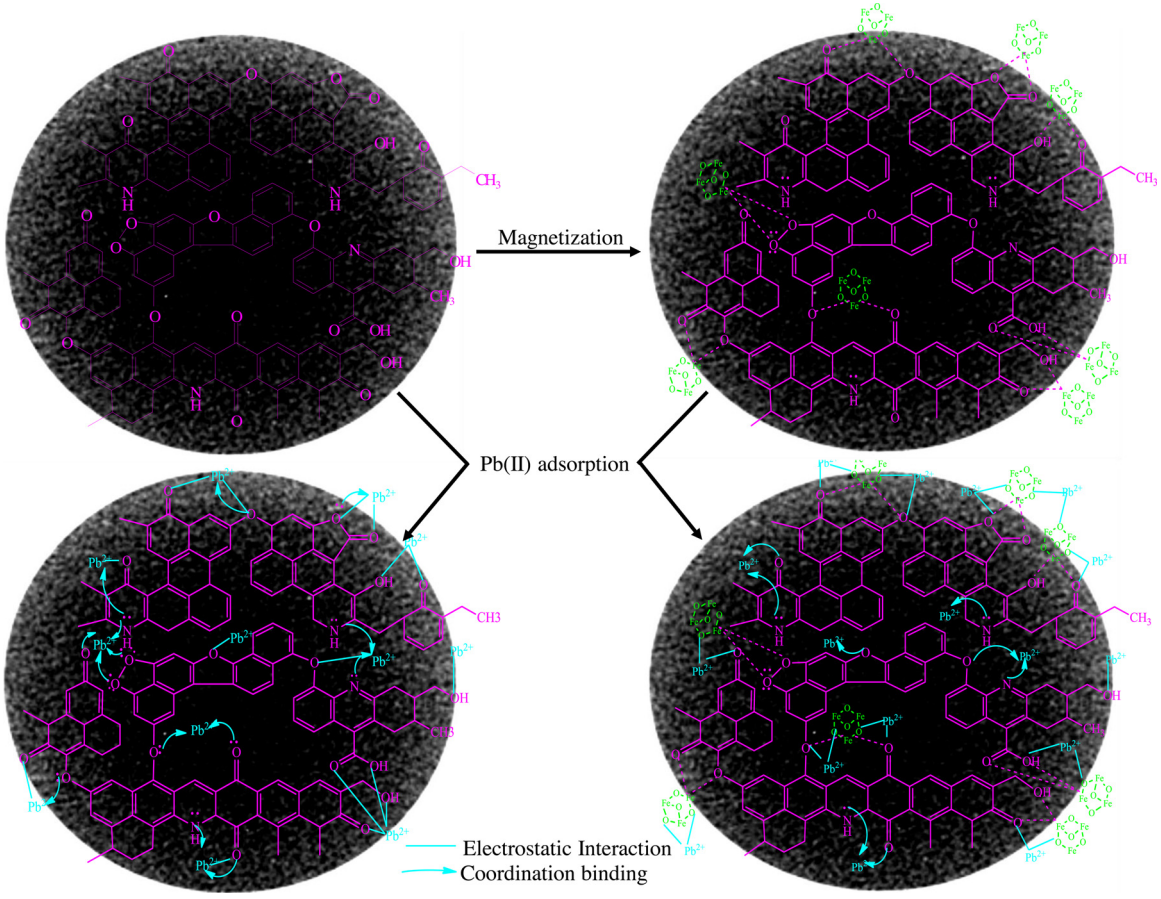

Scheme 1. Synthesis, magnetization, and Pb(II) adsorption mechanism on SOCHC@200C/6 h and mSOCHC@200C/.6 h.

1.0–5.0 kV) and transmission electron microscopy (TEM, Leo 912A 8B OMEGA EF-TEM, Carl Zeiss, Germany, at 120 keV). The X-ray diffraction (XRD, SmartLab, Rigaku) analysis was employed to examine the XRD patterns of samples. The surface characteristics of samples were determined by BET surface area analyzer (3Flex, Micromeritics). The chemical composition of pristine and Pb(II) saturated samples was determined by X-ray photoelectron spectroscopy (XPS, theta probe based system, Thermo Fisher Scientific). The chemical functionalities present on pristine and Pb(II) saturated samples surface were examined by Fourier transform infrared spectrometry (FT-IR, Nicolet 6700, Thermo Scientific). Vibrating sample magnetometer (VSM, PPMS-14, Quantum Design) was used to test the magnetic properties of samples. Themogravimetic analysis (TGA/DTG, Mettler Toledo TGA/SDTA851 with Starc software) in temperature range: 30–800 °C was carried out to test the thermal stability of the samples. The acid (AFC) and base (BFC) functionalities concentrations on HC samples were determined by back titration of the solution (Rao et al., 2010). The point of zero charge (pH_{PZC}) over SOCHC@200 °C/6 h and mSOCHC@200 °C/6 h samples surface was evaluated by solid addition method (Rao et al., 2010).

2.4. Water treatment application

Single metal system batch mode adsorption/desorption experiments were carried out. Stock solution of Pb(II) (C_o: 1000 mg/L) was diluted to prepare solutions of desired concentrations. During pH study, 50 mL of Pb(II) solutions of C_o: 25 mg/L were taken in a series of 100 mL Erlenmeyer flasks and their initial pH (pH_i) was adjusted between ~2 and 7 by adding 0.1 M NaOH/HCl solutions. The solutions were equilibrated with 0.025 g of SOCHC@200 °C/6 h. The contact time (t) study for Pb(II) adsorption was carried out at C_o: 25 mg/L for time range: 1–1440 min. The effect of Pb(II) concentration (C_o: 50–300 mg/L) on adsorption was studied at varied temperature (T: 25–45 °C). The effect of SOCHC@200 °C/6 h concentration (m: 0.01 – 0.075 g) on Pb(II) (C_o: 25 mg/L) adsorption was also studied. At equilibrium, the solid/solution phases were separated through 0.45 μm nylon filter and residual concentrations of Pb(II) were quantitatively analyzed by atomic absorption spectrophotometer (AAS, Perkin Elmer, PinAAcle 900 T). The adsorption capacity at equilibrium (q_e, mg/g), at contact time t (q_t, mg/g), and percentage adsorption (%) were calculated as:

$$q_e = (C_o - C_e) \times \frac{V}{m} \quad (1)$$

$$q_t = (C_o - C_t) \times \frac{V}{m} \quad (2)$$

$$\%Adsorption = \left(\frac{C_o - C_e}{C_o}\right) \times 100 \quad (3)$$

where C_o, C_e, C_t, V, and m are the initial, equilibrium, at any time t concentrations of Pb(II), volume of Pb(II) solution, and amount of SOCHC@200 °C/6 h, respectively.

For Pb(II) recovery, initially, 0.025 g of SOCHC@200 °C/6 h was saturated with 50 mL Pb(II) solution of C_o: 25 mg/L. At equilibrium, solid/solution phases were separated. The saturated SOCHC@200 °C/6 h (solid phases) was washed several times with D.I. water to remove unadsorbed Pb(II) traces, overnight dried at 60 °C. Thereafter, the adsorbed Pb(II) was eluted by using HCl as eluent. Similar elution procedure was repeated using H_2SO_4 and HNO_3 solutions. The concentration of Pb(II) in the eluent was quantitatively analyzed by AAS and the corresponding desorption was calculated as:

$$\%Desorption = \frac{Concentration of Pb(II) desorbed from saturated SOCHC@200°C/6hr}{Concentration of Pb(II) adsorbed on SOCHC@200°C/6hr} \times 100 \quad (4)$$

Comparative experiments following aforementioned protocol were

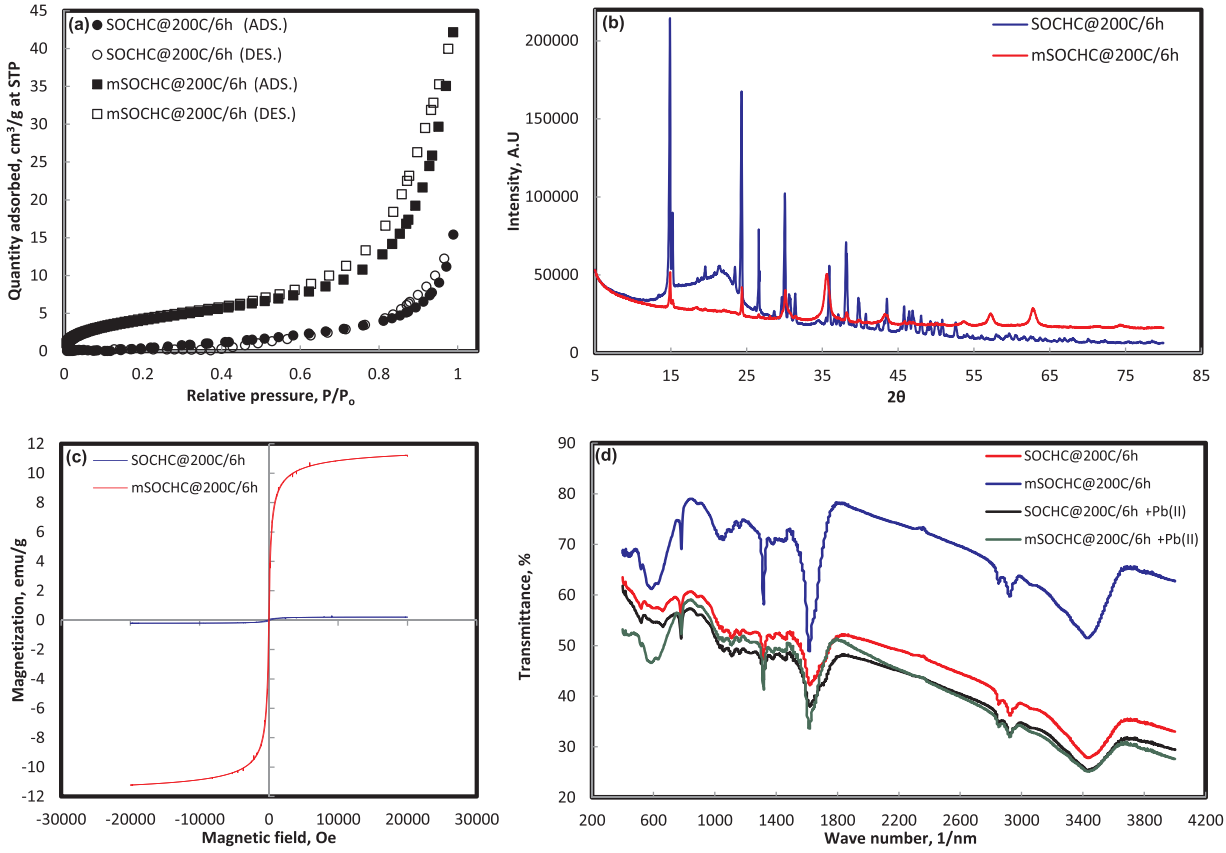

Fig. 1. Nitrogen adsorption/desorption isotherm (a), XRD patterns (b), VSM analysis plot (c), and FT-IR spectra (d).

carried out using mSOCHC@200 °C/6 h as adsorbent. Herein, the solid/solution phases at equilibrium were magnetically separated. Also, the concentration of eluents used during the study was 0.01 M, appropriate enough to restrict iron ions leaching from mSOCHC@200 °C/6 h.

3. Results and discussion

3.1. Optimization of SOCHC developmental conditions

Twelve HC samples (S1 – S12) were developed by varying reaction time (2–8 h) and temperature (150–250 °C), chemically treated with 10 % H_2O_2 to obtain a sample with maximum SOCHC yield and Pb(II) uptake capacity (Table 1). Among the samples developed, highest HC yield was observed for S1 sample (52 %), while lowest yield was found for S12 HC sample (26.5 %). On the other hand, the adsorption of Pb(II) (at C_o: ~15 mg/L) on HC was found to be maximum (24.89 mg/g) for S8 HC sample, while minimum (14.85 mg/g) Pb(II) adsorption was observed on S12 HC sample. However, if both of the aforementioned factors, along with energy consumption and reaction time were together taken into account, S7 HC sample had an upper hand among the developed HC samples with 29.2 % HC yield and 24.57 mg/g Pb(II) adsorption capacity. Therefore, S7 (SOCHC@200 °C/6 h) with BFC and AFC concentrations 0.740 and 1.020 meq./g, respectively was selected for detailed adsorption studies. Further, the optimized sample was magnetized, nomenclature as "mSOCHC@200 °C/6 h".

3.2. Characterization and Pb(II) adsorption mechanism

The N_2 adsorption-desorption isotherm curves of SOCHC@200 °C/6 h and mSOCHC@200 °C/6 h are illustrated in Fig. 1**a**. Conferring to IUPAC classification, type IV curves for both SOCHC@200 °C/6 h and mSOCHC@200 °C/6 h were observed, signifying the presence of mesopores over their respective surfaces. H3-type hysteresis loop ($P/P_o > 0.4$), associated with the presence of slit-shaped pores was only found for mSOCHC@200 °C/6 h (Yusuf et al., 2016). Drastic increase in N_2 adsorption over mSOCHC@200 °C/6 h surface at P/P_o in between 0.8 and 1.0 was observed, hinting towards the existence of macropores (Ma et al., 2015). Thus, both meso and macropores co-exist over mSOCHC@200 °C/6 h surface providing interconnected and low-resistance channels for efficient and rapid Pb(II) diffusion from aqueous phase. The BET surface area of mSOCHC@200 °C/6 h was 15.41 m^2/g (about seventy five-folds higher than SOCHC@200 °C/6 h - 0.20 m^2/g). This shows that magnetization step catalyzes pores development over SOCHC@200 °C/6 h surface, thus, supporting an increase in mSOCHC@200 °C/6 h surface area, favorable for higher Pb(II) adsorption efficiency. Also, nano-sized iron oxide (Fe_xO_y) particles, which were impregnated over SOCHC@200 °C/6 h during magnetization not only favors higher Pb(II) uptake, but also facilitated phase separation after the accomplishment of adsorption process. The single point, t-plot external and Langmuir surface areas of both samples are given in Table 2. After magnetization, an increase in BJH adsorption pore volume (from 0.009 to 0.03 cm^3/g), while a decrease in BJH average adsorption pore diameter (from 4.80 to 4.31 nm) was found.

The XRD patterns of samples are presented in Fig. 1**b**.The SOCHC@200 °C/6 h pattern showed sharp and intense peaks, while a major decrease in peaks intensity was observed for mSOCHC@200 °C/6 h. The 2θ diffraction peaks (indices: h k l) for SOCHC@200 °C/6 h at 14.9 (100), 15.2 (021), 24.3 (040), 26.4 (132), 30.0 (200), 35.6 (104), 38.3 (123), 39.9 (024), and 43.5 (302) depicting pure monoclinic structure, consistent to major crystalline phase of whewellite ($CaC_2O_4{\cdot}H_2O$; ICSD Card No. 01-075-1313). A 2θ diffraction peak at 14.9° in SOCHC@200 °C/6 h XRD pattern, characteristic of cellulose, indicated that 6 h HTC at 200 °C was safe enough to preserve SOC's cellulosic content (Chen et al., 2011). Additionally, a very sharp and intense peak indicates formation of pure crystalline structure of the material due to the removal of hemicellulose and lignin contents (Li et al., 2009). The 2θ diffraction peaks (indices: h k l) with low intensity were observed for mSOCHC@200 °C/6 h at 14.9 (111), 30.1 (220), 35.5 (311), 43.2 (400), 54.0 (422), 57.3 (511), and 62.7 (440), well matched with cubic structure similar to magnetite (Fe_3O_4; ICSD Card No. 01-076-9718). A reduction in typical cellulose peak intensity of mSOCHC@200 °C/6 h confirms crystalline-to-amorphous transition due to magnetite coating over cellulose.

The XRD peaks width was used to calculate the average crystalline size (D_p) of both SOCHC@200 °C/6 h and mSOCHC@200 °C/6 h by employing Debye-Scherrer equation as:

$$D_p(nm) = \frac{K\lambda}{(BCos\theta)} \quad (5)$$

where K is Scherrer constant, λ is X-ray wavelength, B is full width at half maximum of XRD peak, θ is XRD peak position. Estimated D_p magnitudes for SOCHC@200 °C/6 h and mSOCHC@200 °C/6 h were 51.08 and 18.97 nm, respectively.

The VSM analysis plots of SOCHC@200 °C/6 h and mSOCHC@200 °C/6 h are displayed in Fig. 1**c**.For SOCHC@200 °C/6 h, a line almost superimposed to x-axis during VSM analysis was observed, confirming almost negligible magnetic moment while applying magnetic field (i.e. ± 20,000 Oe) at 299.99 K. An S-shaped curve without hesteresis loop was observed for mSOCHC@200 °C/6 h. Also, negligible coercivity and retentivity was observed, indicating its superparamagnetic behavior (Yang et al., 2016). Here, it is noteworthy that superparamagnetic materials in presence of magnetic field behaves as ferromagnetic, while on suppressing magnetic field the particles no longer interact magnetically, thus, preventing agglomeration (Reddy et al., 2012). The saturation magnetization for mSOCHC@200 °C/6 h was11.2 emu/g, good enough for post-adsorption phase separation by an external magnetic field (Saning et al., 2019).

Infra-red (FT-IR) spectrum of SOCHC@200 °C/6 h displayed a broad and strong band, centered at 3410 cm^{-1}, associated with hydroxyl (−OH) group (Fig. 1d). The conjoint bands at 2910 and 2840 cm^{-1} were due to methyl (C–H) group symmetric and asymmetric stretching vibrations. A 1610 cm^{-1} centered broad band was ascribed to aromatic rings of the lignin. A weak band at 1400 cm^{-1} was associated with C—N, present in SOCHC@200 °C/6 h as the nitrogen compounds (Lei et al., 2018) as SOC is rich in protein content. A band at 1317 cm^{-1} was due to the ring breathing vibrations of syringyl units in lignin (Cai et al., 2016). The weak bands between 1000 and 1200 cm^{-1} were due to C—O—C, pointing towards the presence of various oxygen containing functionalities over SOCHC@200 °C/6 h surface. A band at 780 cm^{-1} was assigned to aromatic C–H out-of-plane bending vibrations. After magnetization of SOCHC@200 °C/6 h (mSOCHC@200 °C/6 h), the intensity of bands at 3410, 2910, 2840, 1610, 1317, and 780 cm^{-1} increased. Bondage of respective chemical functionalities with oxides of

Table 2
Surface analysis data summary.

Parameter	Adsorbent	
	SOCHC@200 °C/6 h	mSOCHC@200 °C/6 h
Surface area (SA,m^2/g)		
Single point SA (at P/Po: 0.291)	2.35	14.81
BET SA	0.20	15.41
t-plot External SA	0.26	17.71
Langmuir SA	9.15	32.90
Pore volume (PV,cm^3/g)		
BJH Adsorption cumulative PV (between 0.1 and 300 nm diameter)	0.009	0.03
BJH Desorption cumulative PV (between 0.1 and 300 nm diameter)	0.011	0.04
Pore diameter (PD,nm)		
BJH Adsorption average PD (4 V/A)	4.80	4.31
BJH Desorption average PD (4 V/A)	6.44	5.34

iron during the magnetization step might be a possible reason behind an increase in intensities. Additionally, a new band appeared at 586 cm^{-1} in mSOCHC@200 °C/6 h spectrum, was due to the presence of oxides of iron (Alqadami et al., 2018). A weak band at 460 cm^{-1}, assigned to Si—O—Si stretching vibration in the quartz, observed in SOCHC@200 °C/6 h spectrum, however, it disappeared after magnetization of HC, in-line with previous studies on rice straw developed HC (Liu et al., 2014).After Pb(II) adsorption on SOCHC@200 °C/6 h and mSOCHC@200 °C/6 h, slight shift in bands at 3400, 2910, 2840, 1610, 1317, and 780 cm^{-1} with no or slight decrease in bands intensities was observed.

Morphologically, uneven SOCHC@200 °C/6 h surface with both rough and smooth patches along with some pores was observed (Fig. 2a). Elemental analysis revealed the presence of carbon, oxygen, and nitrogen over SOCHC@200 °C/6 h surface (Fig. 2a, **Inset**). Additionally, TEM analysis of SOCHC@200 °C/6 h showed the presence well dispersed spherical particles (Fig. 2b) with 160 nm average particles size (Fig. 2c). On the other hand, the surface morphology of mSOCHC@200 °C/6 h showed highly porous rough and uneven surface (Fig. 2c), possibly a reason behind its comparatively higher surface area. The elemental analysis showed the presence of iron due to magnetization, along with carbon, oxygen, and nitrogen (Fig. 2c, Inset). The TEM analysis of mSOCHC@200 °C/6 h displayed agglomerated adsorbent particles (Fig. 2e) with 11 nm average particles size (Fig. 2f).

XPS analysis was employed to elucidate chemical species present over pristine and Pb(II) saturated SOCHC@200C/6 h and mSOCHC@200C/6 h surfaces. The overall survey XPS spectrum of SOCHC@200C/6 h showed four major peaks at 531.9, 399.9, 348.2 and 284.7 eV, assigned to oxygen (O 1s), nitrogen (N 1s), calcium (Ca 2p) and carbon (C 1s), respectively (Fig. 3a) (Alqadami et al., 2018). Along with aforementioned peaks, an additional peak, characteristic of iron (Fe 2p), was observed at 710.3 eV binding energy (BE) in mSOCHC@200C/6 h spectrum, confirming that HC was successfully magnetized (Fig. 3a) (Khan et al., 2019a). **Table S1** displayed the atomic contents of pristine and Pb(II) saturated SOCHC@200C/6 h and mSOCHC@200 °C/6 h samples. The deconvoluted Fe 2p spectrum of mSOCHC@200 °C/6 h exhibited two intense peaks at 710.3 and 724.2 eV corresponding to Fe $2p_{3/2}$ and Fe $2p_{1/2}$ spin-orbit peaks of magnetite (Fig. 3a, Inset) (Li et al., 2019). Fig. 3b showed the C1 s spectra of SOCHC@200C/6 h and mSOCHC@200C/6 h were deconvoluted into three peaks at 284.4, 286, 288.1 eV, attributed to C—C/C=C, C—N/C—O, and O—C=O bonds, respectively (Ahmed et al., 2018). After Pb(II) adsorption, a certain increase in C1 s peak intensities was observed (Fig. 3a), confirming the formation of bond through electrostatic attraction between Pb(II) ions and oxygen functionalities attached to carbon atoms. A peak due to O 1s was deconvoluted into three peaks at 529.8, 531, 532.1 eV corresponding to Fe-O, C—O, O=C=O bonds, respectively (Fig. 3c). A nitrogen (N 1s) peak at 399.9 eV was attributed to NH_2 (Fig. 3d). A peak for Pb(II) (Pb 4f) at 143.2 eV, observed in Pb(II) saturated SOCHC@200C/6 h and mSOCHC@200C/6 h samples spectra (Fig. 3a). The Pb 4f exhibited two peaks at 138.5 and 143 eV corresponding to $4f_{7/2}$ and $4f_{5/2}$ (Fig. 3e), derived from spin-orbit splitting. A shift (~1.2 eV) in BE from 139.7 eV (for standard Pb $4f_{7/2}$ spectra of $Pb(NO_3)_2$ sample (Xia et al., 2019)) to 138.5 eV, confirmed strong affinity between SOCHC@200C/6 h/mSOCHC@200C/6 h and Pb(II) ions by newly formed Pb-O groups (Zhang et al., 2017). Also, the Pb 4f BE of Pb(II) ions, adsorbed during the study was much higher than that of PbO (137.2 eV), $Pb(OH)_2$ (137.3 eV), and $PbCO_3$(138.4 eV) (Godelitsas et al., 2003), inferring that the precipitation of Pb(II) as oxide, hydroxide or carbonate was not governing the adsorption process.

During thermogravimetric analysis (TGA) the sample weight losses trends are obtained through TGA curve, while the devolatilization stages are identified by derivative curve (DTG) (Rasapoor et al., 2020). The TGA/DTG thermograms of SOCHC@200C/6 h and mSOCHC@200C/6 h in the temperature range: 25–800 °C were illustrated in Fig. S1 (a and b). Four stage weight losses for both SOCHC@200C/6 h and mSOCHC@200C/6 h were observed. A ~12 (in temperature range: 25–245 °C) and ~5% (in temperature range: 25–158 °C) weight loss was observed from SOCHC@200C/6 h and mSOCHC@200C/6 h during first stage, respectively. This weight loss was due to the evaporation of water molecules and light volatiles (Rasapoor et al., 2020). During second stage, a ~29 % weight loss in temperature range: 245–361 °C was occurred from SOCHC@200C/6 h, while ~15 % weight loss in temperature range: 158–351 °C was occurred from mSOCHC@200C/6 h, attributed to the decomposition of carbohydrates, cellulose, and hemicellulose content from HC samples (Zhou et al., 2015). A third stage weight loss of ~16 % form SOCHC@200C/6 h and ~20 % from mSOCHC@200C/6 h continued till~ 600 °C, ascribed to lignin

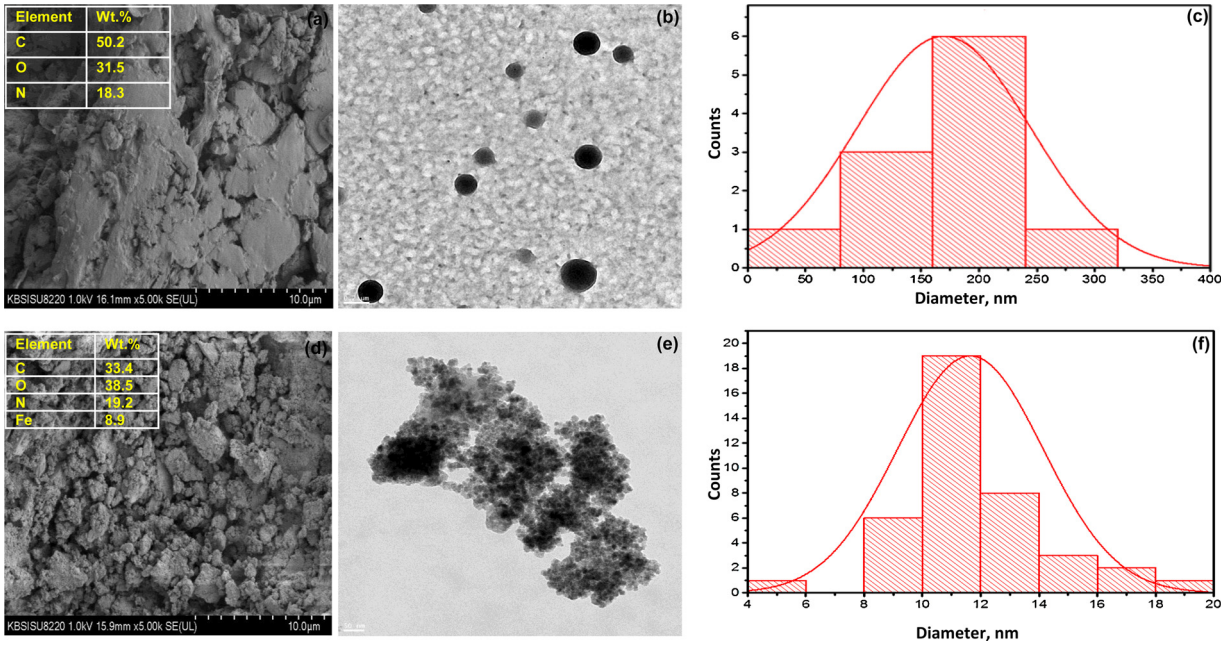

Fig. 2. SEM (Inset: elemental content) (a), TEM (b), and size distribution plot (c) of SOCHC@200 °C/6 h; SEM (Inset: elemental content) (d), TEM (e), and size distribution plot (f) of mSOCHC@200 °C/6 h.

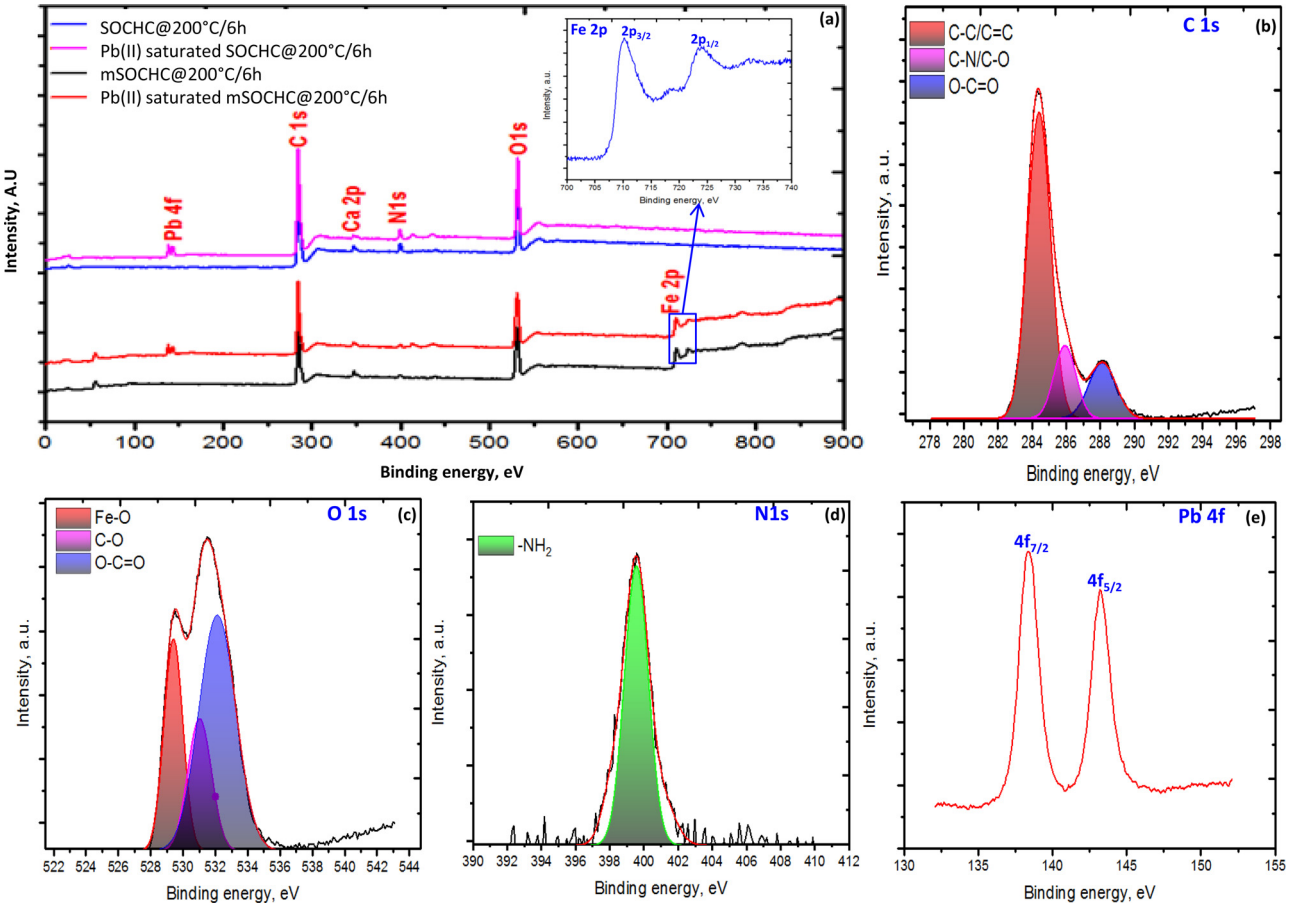

Fig. 3. Wide scan XPS spectra (Inset: deconvoluted XPS spectrum of Fe 2p) **(a)**, Deconvoluted C 1s (b), O 1s (c), N 1s (d), and Pb 4f (e) XPS spectra.

degradation, conversion of hydroxide to oxide, and decomposition of mainly inorganic materials such as oxides and carbonates of calcium (Otero et al., 2011). A minor weight loss during fourth stage between 600 and 800 °C was occurred via devolatilization of residual char and lignin (Yazdani et al., 2019).

As illustrated in Scheme 1 HC was composed of hydrophobic core (darkish in color) and hydrophilic shell (light in color). The outer hydrophilic shell was enriched with oxygen group containing functionalities viz. −OH, −COOH, O−C═O, Fe-O and C═O primarily responsible for binding Pb(II) ions during adsorption. Additionally, the hydrophilic shell also contains some nitrogen group containing functionalities viz. N−H, C−N which also played an active role in Pb(II) adsorption. During adsorption, the cationic Pb(II) ions interact with highly electronegative oxygen atoms through electrostatic interaction and ion-exchange, confirmed by a notable increase in XPS spectra O1 s peak intensity of both SOCHC@200 °C/6 h and mSOCHC@200 °C/6 h (Fig. 3a). Formation of surface complexes due to the sharing of lone pain of electrons of oxygen and nitrogen atoms present on HC surface with Pb(II) might be the other binding possibility, supported by the appearance of new XPS spectral peak at 410 eV BE. This peak provide an evidence of nitrogen atoms involvement in Pb(II) adsorption which results in an increase in the oxidation state due to donating lone pair of electron and thus, the BE of nitrogen atoms (Liu and Bai, 2006). Also, shifting of IR spectral bands for −OH, −COOH, and – NH functionalities during Pb(II) adsorption provide an evidence of their participation during Pb(II) adsorption. In addition, comparatively higher adsorption capacity of Pb(II) on mSOCHC@200C/6 h can be explained by the availability of excessive oxygen binding sites present on magnetite.

3.3. Adsorption studies

3.3.1. Effect of pH on Pb(II) removal

During adsorption, solution pH plays a critical role in sequestering heavy metals ions, especially when electrostatic interactions are the major driving force. In addition, solution pH may influence the adsorption process by dissociating the adsorbate in different species and functionalities present at the adsorbent's active sites (dos Reis et al., 2020a). The adsorption of Pb(II) on both SOCHC@200 °C/6 h and mSOCHC@200 °C/6 h was studied in pH_i range: 1.9–6.7, as above this pH_i value precipitation of Pb(II) was observed (Khan et al., 2019b). Lead adsorption increases linearly in pHi range: 1.9–4.7, attains plateau region in between pH_i 4.7 and 5.5, finally increases slightly in between pHi 5.5 and 6.7 (Fig. 4a). The observed pH_{PZC} values of SOCHC@200 °C/6 h and mSOCHC@200 °C/6 h samples were ~5.41 and 5.38, respectively (**Fig. S2**). The respective adsorption capacities (q_e) of Pb(II) (C_o: 25 mg/L) on SOCHC@200 °C/6 h and mSOCHC@200 °C/6 h at lower pH (pH_i: 4.7) were 42.8 and 45.4 mg/g, finally increased to 44.5 and 48.2 mg/g at pH_i: 6.7, a pH value greater than pH_{PZC} of both samples (at pH > pH_{PZC}, the superficial charges on samples surface become negatively charged (Thue et al., 2020)). Competitive effect between hydronium (H_3O^+) ions and divalent Pb(II) cations to occupy active binding sites on HC surface might result in lesser Pb(II) uptake at lower pH. Conversely, an increase in Pb(II) adsorption was at pH_i: 6.7 was due to a reduction in aqueous phase concentration of interfering H_3O^+ ions. Also, higher pH resulted in deprotonation of the oxygen containing functional groups on HC surface, making them available for binding cationic metal ions.

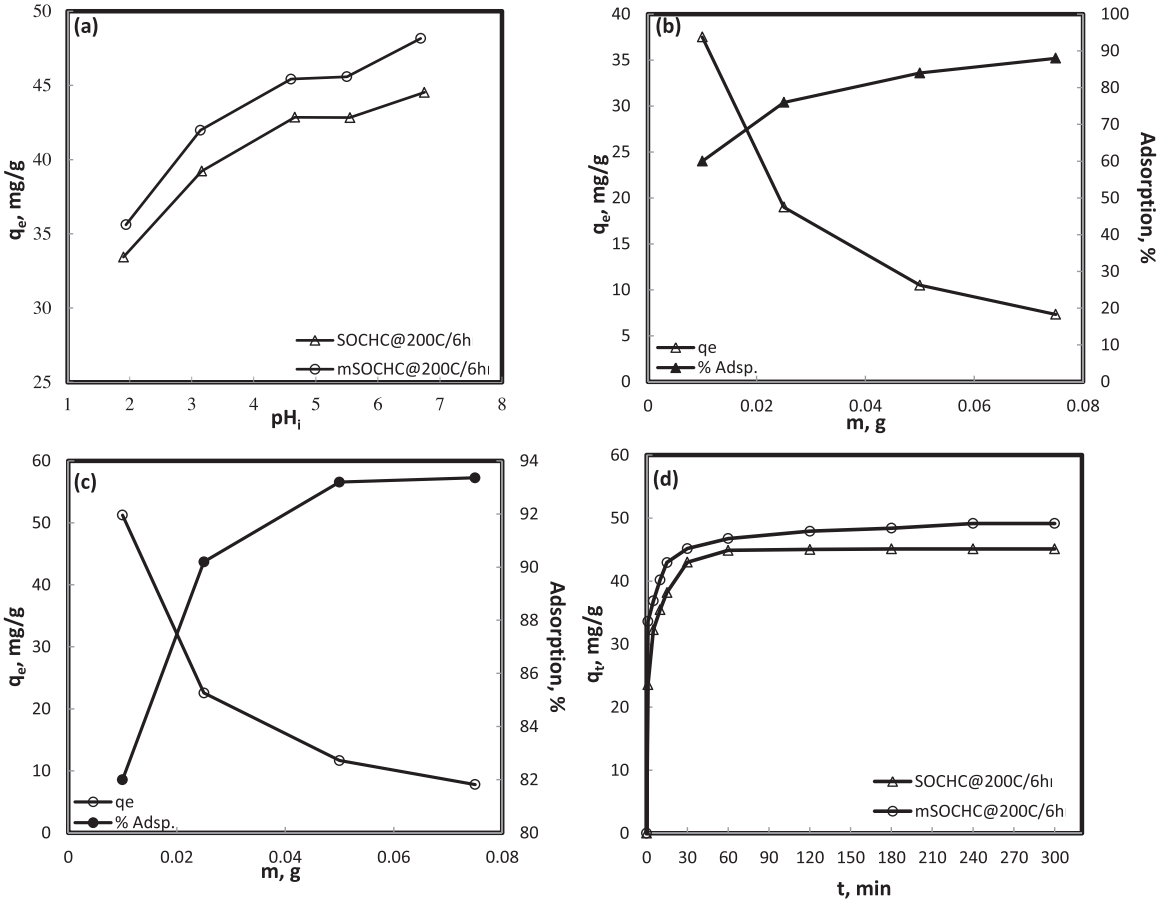

Fig. 4. pH (a), SOCHC@200 °C/6 h dose (b), mSOCHC@200 °C/6 h dose (c), and contact time (d) plots for Pb(II) adsorption.

3.3.2. Effect of adsorbent dosage on Pb(II) removal

The optimization of adsorbent dosage is substantial for aiming maximum removal efficiency while keeping the process cost-effective (dos Reis et al., 2020b). The respective adsorption capacities of Pb(II) at varied SOCHC@200 °C/6 h and mSOCHC@200 °C/6 h doses (0.01 – 0.075 g) decreases from 37.5–7.3 mg/g (Fig. 4b) and 51.2–7.8 mg/g (Fig. 4c). The increase in dose resulted in aggregation of SOCHC@200 °C/6 h and mSOCHC@200 °C/6 h particles in aqueous phase during adsorption. This results a decrease in adsorbent's total surface area and increase diffusional path length (Alsohaimi et al., 2015). While the percentage adsorption of Pb(II) on SOCHC@200 °C/6 h and mSOCHC@200 °C/6 h increases 60–88% and 82–93.4%, respectively. This is attributed to a significant increase in number of available sites for binding Pb(II) present in aqueous solution (dos Reis et al., 2020a).

3.3.3. Effect of contact time on Pb(II) removal

The adsorption of Pb(II) at C_o: 25 mg/L as a function of contact time was studied on both SOCHC@200 °C/6 h and mSOCHC@200 °C/6 h. Extremely rapid Pb(II) uptakes on both SOCHC@200 °C/6 h and mSOCHC@200 °C/6 h were observed, accomplishing 50–70% adsorption within a minute (Fig. 4d). The hydrophilic outer shells along with the co-existence of meso- and macro-porosities over of SOCHC@200 °C/6 h and mSOCHC@200 °C/6 h surfaces are the reason behind rapid Pb (II) uptake (Ünlü and Ersoz, 2006), faster than previously observed Pb (II) uptake on mSBHC-N (Khan et al., 2019a). This proposes their potential usage in continuous flow industrial water treatment columns. The equilibration time for Pb(II) adsorption on SOCHC@200 °C/6 h was 180 min (3 h) with q_e – 45.1 mg/g, while the equilibration time on mSOCHC@200 °C/6 h was 240 min (4 h) with q_e – 49.2 mg/g. The synergic effect of oxygen and iron containing functionalities, as depicted by FT-IR and XPS analysis, might be responsible for higher magnitude of q_e for Pb(II) on mSOCHC@200 °C/6 h.

3.3.4. Effect of concentration on Pb(II) removal at varied temperature

The adsorption of Pb(II) on both SOCHC@200 °C/6 h and mSOCHC@200 °C/6 h was studied as a function of initial concentration (C_o): 50–300 mg/L at varied temperature (T): 298–318 K. The adsorption of Pb(II) at 298 K on SOCHC@200 °C/6 h increased from 89.2–271 mg/g, while on mSOCHC@200 °C/6 h the adsorption increased from 93.8–334 mg/g. At 308 K, the adsorption of Pb(II) on SOCHC@200 °C/6 h increased from 69.9–220.6 mg/g, while on mSOCHC@200 °C/6 h the adsorption increased from 78.9–294.8 mg/g. At 318 K, the adsorption of Pb(II) on SOCHC@200 °C/6 h increased from 52–183.2 mg/g, while on mSOCHC@200 °C/6 h the adsorption increased from 67.7–253.6 mg/g. Overall, the adsorption increases with increase in concentration. However, a decrease in adsorption with increase in temperature was observed confirming exothermic adsorption process.

3.4. Adsorption modeling

3.4.1. Kinetic modeling

Pseudo-first-order (PFO), pseudo-second-order (PSO), and intra-particle diffusion (IPD) models were applied to evaluate the experimental data. The models details are given in supplementary information (**Text S1** [53]) and parameters are presented in Table 3. PFO model assumes that the diffusion of adsorbate ions dominates the adsorption velocity, while PSO bank on assumption that chemisorption through sharing or exchange of ions between adsorbate and adsorbent limits the step rate (Zhou et al., 2017). Higher regression coefficient (R^2) and nearer $q_{e,cal.}$ and $q_{e,exp.}$ values supported the applicability of PSO model.

Table 3
Kinetic data for Pb(II) adsorption on SOCHC@200 ˚C/6 h and mSOCHC@200 ˚C/6 h.

Model	Adsorbent	
	SOCHC@200C/6 h	mSOCHC@200C/6 h
PFO		
$k_{1,\ 1/min}$	0.0479	0.0159
$q_{e,cal.}$, mg/g	13.32	9.69
R^2	0.9111	0.8947
PSO		
$k_{2,\ g/mg\text{-}min}$	0.0123	0.0087
$q_{e,cal.}$, mg/g	45.45	49.50
h, mg/g-min	25.45	21.32
R^2	1	0.9999
IPD		
k_{IPD}, mg/g-$min^{1/2}$	0.9953	0.3708
I	31.74	39.66
R^2	0.6277	0.5148
$q_{e,exp.}$	45.11	49.16

Results suggest that chemical forces were involved during the adsorption of Pb(II) on SOCHC@200 ˚C/6 h and mSOCHC@200 ˚C/6 h. The magnitude of initial sorption rate constant (h) was comparatively higher for SOCHC@200 ˚C/6 h. This showed that though better Pb(II) uptake was observed over mSOCHC@200 ˚C/6 h, however, during initial stage the Pb(II) uptake was rapid on SOCHC@200 ˚C/6 h.The IPD plots for Pb(II) adsorption on SOCHC@200 ˚C/6 h and mSOCHC@200 ˚C/6 h showed multi-step linearity (**Fig. S3**), revealing that the adsorption process was governed by two or more steps viz. boundary layer (external) diffusion, and intra-particle (internal) diffusion. The initial sharper slopes of the plots were attributed to the transportation of Pb (II)from the bulk to SOCHC@200 ˚C/6 h and mSOCHC@200 ˚C/6 h surfaces. During this process a boundary layer present around the adsorbent surface was involved. The second and final portion of the plot describes gradual adsorption stage, corresponding to Pb(II) diffusion inside the pores (meso and macro-pores) on SOCHC@200 ˚C/6 h and mSOCHC@200 ˚C/6 h surface (intra-particle diffusion). The gradual adsorption during second stage indicates that it was a rate-limiting step. The magnitudes of IPD constant (K_{IPD}) for Pb(II) adsorption on SOCHC@200 ˚C/6 h and mSOCHC@200 ˚C/6 h were 0.9953 and 0.3708 mg/g-$min^{1/2}$, respectively. The respective magnitudes of boundary layer thickness (I) for Pb(II) adsorption on SOCHC@200 ˚C/6 h and mSOCHC@200 ˚C/6 h were 31.74 and 39.66, attributing to greater effect of boundary layer on Pb(II) adsorption onto mSOCHC@200 ˚C/6 h.

3.4.2. Isotherm modeling

Non-linear Langmuir, Freundlich, and Temkin isotherm models were applied to Pb(II) adsorption data on SOCHC@200 ˚C/6 h and mSOCHC@200 ˚C/6 h at varied temperatures (T: 25–45 ˚C).The model details are given in supplementary information (**Text S2** Khan et al., 2012). The respective non-linear adsorption isotherm plots and calculated parameters are illustrated in **Fig. S4**, **S5**, and Table 4. Adsorption of Pb(II) on both SOCHC@200 ˚C/6 h and mSOCHC@200 ˚C/6 h was fitted to Langmuir isotherm model, depicted by higher R^2, and almost superimposed $q_{e,\ exp.}$ and $q_{e,\ cal.}$ values (from non-linear isotherm plots **Fig. S4** and **S5**). Further, to validate the applicability of Langmuir model two additional error functions, namely the sum of the squares of errors (ERRSQ) and the hybrid fractional error function (HYBRID) (Details in supplementary data, **Text S3**) were applied to adsorption isotherms data. The parameter sets providing the lowest normalized error for Langmuir isotherm model, confirming fitting of the model, in line with previous results of Pb(II)adsorption on rice husk HC (Teng et al., 2020). The maximum monolayer adsorption capacities (q_m) for Pb(II) adsorption on both SOCHC@200 ˚C/6 h and mSOCHC@200 ˚C/6 h at 25 ˚C were 304.9 and 361.7 mg/g, decreases to 273.8 and 331.1 mg/g with increases in temperature to 45 ˚C. The observed q_m values for Pb(II) adsorption on mSOCHC@200 ˚C/6 h at 25 ˚C were comparatively better than other magnetic biochars (Table 5).The values of Freundlich constant (n) were in range of favorable adsorption.

3.4.3. Thermodynamic modeling

The thermodynamic parameters, viz. standard free energy change (ΔG˚, kJ/mol), standard enthalpy change (ΔH˚, kJ/mol), and standard entropy change (ΔS˚, J/mol-K) for the adsorption of Pb(II) on SOCHC@200 ˚C/6 h and mSOCHC@200 ˚C/6 h were evaluated using equations as (Khan et al., 2020):

$$\Delta G^{\circ} = -RTln(K_e^0) \tag{6}$$

$$ln(K_e^0) = \frac{\Delta S^{\circ}}{R} - \frac{\Delta H^{\circ}}{R} \times \frac{1}{T} \tag{7}$$

where K_e^o (dimensionless) is the thermodynamic equilibrium constant at specified temperature, R (8.314 J/K-mol) is the universal gas

Table 4
Isotherm data for Pb(II) adsorption on SOCHC@200 ˚C/6 h and mSOCHC@200 ˚C/6 h.

Isotherm	Temperature, ˚C					
	25		35		45	
	SOCHC@200 ˚C/6 h	mSOCHC@200 ˚C/6 h	SOCHC@200 ˚C/6 h	mSOCHC@200 ˚C/6 h	SOCHC@200 ˚C/6 h	mSOCHC@200 ˚C/6 h
Langmuir						
q_m, mg/g	304.9	361.7	284.8	339.9	273.8	331.1
K_L, L/mg	0.0698	0.0889	0.0228	0.0381	0.0107	0.0189
R^2	**0.9914**	**0.9990**	**0.9809**	**0.9822**	**0.9850**	**0.9912**
ERRSQ	**489.8**	**441.5**	**324.7**	**492.6**	**184.4**	**196.4**
HYBRID	**2.44**	**2.65**	**1.95**	**4.96**	**1.63**	**2.04**
Freundlich						
K_F, (mg/g) (L/mg)$^{1/n}$	65.4	83.0	27.0	36.6	5.3	19.6
n	3.2862	3.2927	2.3669	2.2805	1.4227	1.9357
R^2	0.8835	0.9371	0.9120	0.9286	0.8969	0.9515
ERRSQ	3665.3	2920.5	1756.7	2882.6	2510.3	1396.4
HYBRID	17.25	14.02	10.80	15.88	15.76	8.48
Temkin						
B_T	31.4	68.2	26.3	48.3	24.2	38.1
K_T, L/mg	38.452	1.265	36.414	1.111	29.816	0.940
R^2	0.5351	0.9843	0.4296	0.6204	0.2947	0.4561
ERRSQ	8591.7	720.4	14766.7	8614.6	22504.7	10829.3
HYBRID	83.25	2.80	173.91	46.20	314.41	60.12

Table 5
Maximum monolayer adsorption capacities (q_m) comparison of different magnetic biochars for Pb(II) removal.

Adsorbent	Experiment conditions	q_m, mg/g	Reference
Magnetic vinasse and red mud HC	C_o: 25 − 500 mg/L; pH: 5.5; t: 120 min; T: 25 °C	223.1	(Kazak and Tor, 2020)
Magnetic bone BC	C_o: 25–250 mg/L; pH: 5.7; t: 120 min; T: 25 °C	344.8	(Alqadami et al., 2018)
Magnetic sugarcane bagasse HC	C_o: 25–400 mg/L; pH: 6.5; t: 180 min; T: 25 °C	222.2	(Khan et al., 2019a)
Magnetic pinewood sawdust HC	C_o: 1–200 mg/L; pH: 5 ± 0.05; T: 25 °C	92.8	(Xia et al., 2019)
SOCHC@200 °C/6 h	C_o: 50–300 mg/L; pH: 6.7; T: 25 °C; t: 180 min	304.9	This study
mSOCHC@200 °C/6 h	C_o: 50–300 mg/L; pH: 6.7; T: 25 °C ; t: 240 min	361.7	This study

constant, T (K) is the absolute temperature.

The thermodynamic equilibrium constant (K_e^o) is calculated as (Thue et al., 2018; Lima et al., 2019):

$$K_e^o = \frac{(1000 \times K_g \times Molecularweightofadsorbate) \times [Adsorbate]^o}{\gamma} \quad (8)$$

where γ (dimensionless) is the activity coefficient, [Adsorbate]^o (1 mol/L) is the unitary standard concentration of adsorbate, K_g (L/mol) is the best fitted isotherm model (Langmuir is the best fitted model during present study, therefore $K_g = K_L$), K_L is a Langmuir constant related to heat of adsorption. ΔS° and ΔH° were calculated from the intercept and slope of Van't Hoff plot (lnK_e^o versus $1/T$, plots not shown).

The adsorption of Pb(II) on both SOCHC@200 °C/6 h and mSOCHC@200 °C/6 h was exothermic, depicted by negative ΔH° values (Table 6). The ΔH° magnitude for Pb(II) uptake on both SOCHC@200 °C/6 h and mSOCHC@200 °C/6 h was in range of physical adsorption (≤ 40 kJ/mol) (Bandegharaei et al., 2019). The randomness/disturbance at solid-solution phase (depicted by positive ΔS° values) was observed during Pb(II) adsorption on SOCHC@200 °C/6 h and mSOCHC@200 °C/6 h (Lima et al., 2015). This randomness might occur due to redistribution of rational and transitional energies between the phases. The ΔG° values for the adsorption of Pb(II) on SOCHC@200 °C/6 h and mSOCHC@200 °C/6 h at varied temperatures were negative, indicative of spontaneous adsorption process. The negative magnitude of ΔG° decreases with increase in temperature, indicating that Pb(II) adsorption on both SOCHC@200 °C/6 h and mSOCHC@200 °C/6 h was energetically not favored (Wamba et al., 2017).

3.5. Desorption studies

Regeneration of adsorbent and recovery of analyte are the major goals to be achieved during desorption studies (dos Reis et al., 2016). The strong acids (HCl, HNO_3, and H_2SO_4) solutions of C_o: 0.01 M were used to recover Pb(II) from saturated SOCHC@200 °C/6 h and mSOCHC@200 °C/6 h. The recovery of Pb(II) from both SOCHC@200 °C/6 h and mSOCHC@200 °C/6 h followed the order: HCl > HNO_3 > H_2SO_4 (**Fig. S6**). This shows that ionic size of eluents played a critical role in Pb(II) elution from saturated SOCHC@200 °C/6 h and mSOCHC@200 °C/6 h. Chloride ion (Cl^-) being smallest, thus, maximum Pb(II) ions were eluted by HCl. However, higher (92.2 %) amount of Pb(II) was recovered with mSOCHC@200 °C/6 h compared to 88.9 % Pb(II) recovery by SOCHC@200 °C/6 h.

4. Conclusions

Sesame oil cake hydrochar (SOCHC) sample developed at reaction temperature 200 °C and time 6 h, chemically modified with 10 % H_2O_2 (SOCHC@200 °C/6 h) with maximum Pb(II) removal and fairly high HC yield was optimized for adsorption studies. Further, the optimized SOCHC@200 °C/6 h sample was magnetized (mSOCHC@200 °C/6 h) through co-precipitation methodology. The SOCHC@200 °C/6 h surface was mesoporous, while both meso- and macropores co-exists over mSOCHC@200 °C/6 h which was magnetically superparamagnetic. Oxygen functionalities enriched pristine SOCHC@200 °C/6 h and mSOCHC@200 °C/6 h surfaces were revealed during IR analysis. The XPS spectral peak at BE 710.3 eV affirmed magnetization of SOCHC@200 °C/6 h, while a peaks at BEs 143.2 eV depicted adsorption of Pb(II) on both SOCHC@200 °C/6 h and mSOCHC@200 °C/6 h surfaces. Contact time, pH, initial concentration, and temperature dependent Pb (II) adsorption was observed. Adsorption data was fitted to Langmuir isotherm and PFO kinetics models. IPD plot showed multi-step linearity revealing that the adsorption process was governed by two or more steps. The q_m value for Pb(II) adsorption at 25 °C were comparatively higher for mSOCHC@200 °C/6 h (361.7 mg/g) than SOCHC@200 °C/6 h (304.9 mg/g). Maximum amount of Pb(II) from both SOCHC@200 °C/6 h (92.2 %) and mSOCHC@200 °C/6 h (88.9 %) was eluted with 0.01 M HCl. Conclusively, if uptake and separation ease considered mSOCHC@200 °C/6 h was a better adsorbent for Pb(II) removal, while if adsorption kinetics and elution efficiency was considered SOCHC@200 °C/6 h gives better results.

CRediT authorship contribution statement

Moonis Ali Khan: Conceptualization, Supervision, Writing - original draft, Funding acquisition. **Ayoub Abdullah Alqadami:** Data curation, Formal analysis. **Saikh Mohammad Wabaidur:** Software, Validation. **Masoom Raza Siddiqui:** Methodology, Investigation. **Byong-Hun Jeon:** Writing - review & editing. **Shareefa Ahmed Alshareef:** Methodology, Investigation. **Zeid A. Alothman:** Project administration. **Abdelrazig Elfaki Hamedelniel:** Writing - review & editing.

Declaration of Competing Interest

The authors declare that they have no known competing financial interests or personal relationships that could have appeared to influence the work reported in this paper.

Acknowledgement

The authors would like to extend their sincere appreciation to the Deanship of Scientific Research at King Saud University for funding this work through the research group No. RG-1437-031. BHJ is thankful for the financial support (No. 2018002480007) from the Korea Environmental Technology Institute (KEITI) and the Ministry of Environment (ME) of the Republic of Korea.

Table 6
Thermodynamics parameters for Pb(II) adsorption on SOCHC@200 °C/6 h and mSOCHC@200 °C/6 h.

Adsorbent	Parameters				
	ΔH°, J/mol	ΔS°, J/mol-K	ΔG°, kJ/mol		
			298K	308K	318 K
SOCHC@200 °C/6 h	−0.0008	0.031	−23.73	−21.66	−20.37
mSOCHC@200 °C/6 h	−0.0008	0.017	−24.33	−22.98	−21.87

Appendix A. Supplementary data

Supplementary material related to this article can be found, in the online version, at doi:https://doi.org/10.1016/j.jhazmat.2020.123247.

References

Ahmed, M.B., Zhou, J.L., Ngo, H.H., Johir, M.A.H., Sornalingam, K., 2018. Sorptive removal of phenolic endocrine disruptors by functionalized biochar: Competitive interaction mechanism, removal efficacy and application in wastewater. Chem. Eng. J. 335, 801–811.

Ajmal, M., Rao, R.A.K., Khan, M.A., 2005. Adsorption of copper from aqueous solution on *Brassica cumpestris* (mustard oil cake). J. Hazard. Mater. B 122, 177–183.

Alqadami, A.A., Khan, M.A., Otero, M., Siddiqui, M.R., Jeon, B.-H., Batoo, K.M., 2018. A magnetic nanocomposite produced from camel bones for an efficient adsorption of toxic metals from water. J. Clean. Prod. 178, 293–304.

Alsohaimi, I.H., Khan, M.A., Alothman, Z.A., Khan, M.R., Kumar, M., Almahri, A.M., 2015. Synthesis, characterization, and application of Fe-CNTs nanocomposite for BrO_3^- remediation from water samples. J. Ind. Eng. Chem. 26, 218–225.

Bandegharaei, D.R.Lima A.H., Thue, P.S., Lima, E.C., de Albuquerque, Y.R.T., dos Reis, G.S., Umpierres, C.S., Dias, S.L.P., Tran, H.N., 2019. Efficient acetaminophen removal from water and hospital effluents treatment by activated carbons derived from Brazil nutshells. Colloids Surf. A Physicochem. Eng. Asp. 583, 123966.

Bedigian, D., Harlan, J.R., 1986. Evidence for cultivation of sesame in the ancient world. Economic Bot. 40 (2), 137–154.

Cai, J., Li, B., Chen, C., Wang, J., Zhao, M., Zhang, K., 2016. Hydrothermal carbonization of tobacco stalk for fuel application. Bioresour. Technol. Rep. 220, 305–311.

Chen, W., Yu, H., Liu, Y., Chen, P., Zhang, M., Hai, Y., 2011. Individualization of cellulose nanofibers from wood using high-intensity ultrasonication combined with chemical pretreatments. Carb. Poly. 83, 1804–1811.

Daneshvar, N., Salari, D., Aber, S., 2002. Chromium adsorption and Cr(VI) reduction to trivalent chromium in aqueous solutions by soya cake. J. Hazard. Mater. 94 (1), 49–61.

dos Reis, G.S., Adebayo, M.A., Lima, E.C., Sampaio, C.H., Prola, L.D.T., 2016. Activated carbon from sewage sludge for preconcentration of copper. Anal. Lett. 49 (4), 541–555.

dos Reis, G.S., Thue, P.S., Cazacliu, B.G., Lima, E.C., Sampaio, C.H., Quattrone, M., Ovsyannikova, E., Kruse, A., Dotto, G.L., 2020a. Effect of concrete carbonation on phosphate removal through adsorption process and its potential application as fertilizer. J. Clean. Prod. 256, 120416.

dos Reis, G.S., Cazacliu, B.G., Correa, C.R., Ovsyannikova, E., Kruse, A., Sampaio, C.H., Lima, E.C., Dotto, G.L., 2020b. Adsorption and recovery of phosphate from aqueous solution by the construction and demolition wastes sludge and its potential use as phosphate-based fertilizer. J. Environ. Chem. Eng. 8, 103605.

Fernandez, M.E., Ledesma, B., Román, S., Bonelli, P.R., Cukierman, A.L., 2015. Development and characterization of activated hydrochars from orange peels as potential adsorbents for emerging organic contaminants. Bioresour. Technol. Rep. 183, 221–228.

Godelitsas, A., Astilleros, J.M., Hallam, K., Harissopoulos, S., Putnis, A., 2003. Interaction of calcium carbonates with lead in aqueous solutions. Environ. Sci. Technol. 37 (15), 3351–3360.

Hu, W., Tong, W., Y.Li, Y.Xie, Chen, Y., Wen, Z., Feng, S., Wang, X., Li, P., Wang, Y., Zhang, Y., 2020. Hydrothermal route-enabled synthesis of sludge-derived carbon with oxygenfunctional groups for bisphenol A degradation through activation of peroxymonosulfate. J. Hazard. Mater. 388, 121801.

Kambo, H.S., Dutta, A., 2015. A comparative review of biochar and hydrochar in terms of production, physico-chemical properties and applications. Renewable Sustainable Energy Rev. 45, 359–378.

Karagöz, S., Tay, T., Ucar, S., Erdem, M., 2008. Activated carbons from waste biomass by sulfuric acid activation and their use on methylene blue adsorption. Bioresour. Technol. Rep. 99, 6214–6222.

Kazak, O., Tor, A., 2020. In situ preparation of magnetic hydrochar by co-hydrothermal treatment of waste vinasse with red mud and its adsorption property for Pb(II) in aqueous solution. J. Hazard. Mater. 393, 122391.

Khan, M.A., Ngabura, M., Choong, T.S., Masood, H., Chuah, L.A., 2012. Biosorption and desorption of nickel on oil cake: batch and column studies. Bioresour. Technol. 103, 35–42.

Khan, M.A., Alqadami, A.A., Otero, M., Siddiqui, M.R., Alothman, Z.A., Alsohaimi, I., Rafatullah, M., Hamedelnie, A.E., 2019a. Heteroatom-doped magnetic hydrochar to remove post-transition and transition metals from water: synthesis, characterization, and adsorption studies. Chemosphere 218, 1089–1099.

Khan, M.A., Otero, M., Kazi, M., Alqadami, A.A., Wabaidur, S.M., Siddiqui, M.R., Alothman, Z.A., Sumbul, S., 2019b. Unary and binary adsorption studies of lead and malachite green onto a nanomagnetic copper ferrite/drumstick pod biomass composite. J. Hazard. Mater. 365, 759–770.

Khan, M.A., Wabaidur, S.M., Siddiqui, M.R., Alqadami, A.A., Khan, A.H., 2020. Silico-manganese fumes waste encapsulated cryogenic alginate beads for aqueous environment de-colorization. J. Clean. Prod. 244, 118867.

Konstantinou, M., Kolokassidou, K., Pashalidis, I., 2007. Sorption of Cu(II) and Eu(III) ions from aqueous solution by olive cake. Adsorption 13 (1), 33–40.

Kumar, G.V.S.R.P., Malla, K.A., Yerra, B., Rao, K.S., 2019. Removal of Cu(II) using three low-cost adsorbents and prediction of adsorption using artificial neural networks. Appl. Water Sci. 9, 44.

Kuo, L.H., 1967. Animal feeding stuffs compositional data of feeds and concentrates (part 3). Malaysian Agri. J. 46, 63–70.

Lei, Y., Su, H., Tian, F., 2018. A novel nitrogen enriched hydrochar adsorbents derived from salix biomass for Cr (VI) adsorption. Sci. Rep. 8, 4040.

Li, R., Fei, J., Cai, Y., Li, Y., Feng, J., Yao, J., 2009. Cellulose whiskers extracted from mulberry: a novel biomass production. Carb. Poly. 76 (1), 94–99.

Li, S., Wang, Z., Zhao, X., Yang, X., Liang, G., Xie, X., 2019. Insight into enhanced carbamazepine photodegradation over biochar-based magnetic photocatalyst Fe_3O_4/BiOBr/BC under visible LED light irradiation. Chem. Eng. J. 360, 600–611.

Lima, É.C., Adebayo, M.A., Machado, F.M., 2015. Kinetic and Equilibrium Models of Adsorption, Carbon Nanomaterials As Adsorbents for Environmental and Biological Applications. Springer, pp. 33–69.

Lima, É.C., Hosseini-Bandegharaei, A., Moreno-Piraján, J.C., Anastopoulos, I., 2019. A critical review of the estimation of the thermodynamic parameters on adsorption equilibria. Wrong use of equilibrium constant in the Van't Hoff equation for calculation of thermodynamic parameters of adsorption. J. Mol. Liq. 273, 425–434.

Liu, C., Bai, R., 2006. Adsorptive removal of copper ions with highly porous chitosan/cellulose acetate blend hollow fiber membranes. J. Membrane Sci. 284, 313–322.

Liu, Y., Zhu, X., Qian, F., Zhang, S., Chen, J., 2014. Magnetic activated carbon prepared from rice straw-derived hydrochar for triclosan removal. RSC Adv. 4, 63620.

Ma, H., Li, J.-B., Liu, W.-W., Miao, M., Cheng, B.-J., Zhu, S.-W., 2015. Novel synthesis of a versatile magnetic adsorbent derived from corncob for dye removal. Bioresour. Technol. Rep. 190, 13–20.

Nagashanmugam, K.B., 2018. Evaluation of chromium (VI) removal by carbons derived from *Sesamum indicum* oil cake. J. South African Inst. Mining Metal. 118 (4), 369–376.

Nagashanmugam, K.B., Srinivasan, K., 2010. Evaluation of Lead(II) removal by carbon derived from gingelly oil cake. Asian J. Chem. 22 (7), 5447–5462.

Oliver-Tomas, B., Hitzl, M., Owsianiak, M., Renz, M., 2019. Evaluation of hydrothermal carbonization in urban mining for the recovery of phosphorus from the organic fraction of municipal solid waste. Resour. Conver. Recycl. 147, 111–118.

Otero, M., Lobato, A., Cuetos, M.J., Sánchez, M.E., Gómez, X., 2011. Digestion of cattle manure: thermogravimetric kinetic analysis for the evaluation of organic matter conversion. Biores.Technol. 102, 3404–3410.

Rao, R.A.K., Khan, M.A., 2007. Removal and recovery of Cu(II), Cd(II) and Pb(II) ions from single and multimetal systems by batch and column operation on neem oil cake (NOC). Sep. Purif. Technol. 57, 394–402.

Rao, R.A.K., Khan, M.A., Jeon, B.-H., 2010. Utilization of carbon derived from mustard oil cake (CMOC) for the removal of bivalent metal ions: effect of anionic surfactant on the removal and recovery. J. Hazard. Mater. 173, 273–282.

Rasapoor, M., Young, B., Asadov, A., Brar, R., Sarmah, A.K., Zhuang, W.Q., Baroutian, S., 2020. Effects of biochar and activated carbon on biogas generation: a thermogravimetric and chemical analysis approach. Energy Conser. Manag. 203, 112221.

Reddy, L.H., Arias, J.L., Nicolas, J., Couvreur, P., 2012. Magnetic nanoparticles: design and characterization, toxicity and biocompatibility, pharmaceutical and biomedical applications. Chem. Rev. 112, 5818–5878.

Román, S., Nabais, J.M.V., Ledesma, B., González, J.F., Laginhas, C., Titirici, M.M., 2013. Production of low-cost adsorbents with tunable surface chemistry by conjunction of hydrothermal carbonization and activation processes. Microporous Mesoporous Mater. 165, 127–133.

Sánchez-Cantú, M., Janeiro-Coronel, V.J., Galicia-Aguilar, J.A., Santamaría-Juárez, J.D., 2018. Effect of the activation temperature over activated carbon production from castor cake and its evaluation as dye adsorbent. Int. J. Environ. Sci. Technol. (Tehran) 15 (7), 1521–1530.

Saning, A., Herou, S., Dechtrirat, D., Ieosakulrat, C., Pakawatpanurut, P., Kaowphong, S., Thanachayanont, C., Titirici, M.-M., Chuenchom, L., 2019. Green and sustainable zero-waste conversion of water hyacinth (*Eichhornia crassipes*) into superior magnetic carbon composite adsorbents and supercapacitor electrodes. RSC Adv. 9, 24248–24258.

Shanmugaprakash, M., Sivakumar, V., 2015. Batch and fixed-bed column studies for biosorption of Zn(II) ions onto *pongamia* oil cake (*Pongamiapinnata*) from biodiesel oil extraction. J. Environ. Manag 164, 161–170.

Spataru, A., Jain, R., Chung, J.W., Gerner, G., Krebs, R., Lens, P.N.L., 2016. Enhanced adsorption of orthophosphate and copper onto hydrochar derived from sewage sludge by KOH activation. RSC Adv. 6, 101827–101834.

Teng, F., Zhang, Y., Wang, D., Shen, M., Hu, D., 2020. Iron-modified rice husk hydrochar and its immobilization effect for Pb and Sb in contaminated soil. J. Hazard. Mater. 398, 122977.

Thue, P.S., Sophia, A.C., Lima, E.C., Wamba, A.G., de Alencar, W.S., dos Reis, G.S., Rodembusch, F.S., Dias, S.L., 2018. Synthesis and characterization of a novel organic-inorganic hybrid clay adsorbent for the removal of acid red 1 and acid green 25 from aqueous solutions. J. Clean. Prod. 171, 30–44.

Thue, P.S., Umpierres, C.S., Lima, E.C., Lima, D.R., Machado, F.M., dos Reis, G.S., da Silva, R.S., Pavan, F.A., Tran, H.N., 2020. Single-step pyrolysis for producing magnetic activated carbon from tucumã (*Astrocaryum aculeatum*) seed and nickel(II) chloride and zinc(II) chloride. Application for removal of nicotinamide and propranolol. J. Hazard. Mater. 398, 122903.

Tran, T.H., Le, A.H., Pham, T.H., Nguyen, D.T., Chang, S.W., Chung, W.J., Nguyen, D.D., 2020. Adsorption isotherms and kinetic modeling of methylene blue dye onto a carbonaceous hydrochar adsorbent derived from coffee husk waste. Science of the Tot. Env. 725, 138325.

Uçar, S., Erdem, M., Tay, T., Karagöz, S., 2015. Removal of lead (II) and nickel (II) ions from aqueous solution using activated carbon prepared from rapeseed oil cake by Na_2CO3 activation. Clean Technol. Environ. Pol. 17 (3), 747–756.

Ünlü, N., Ersoz, M., 2006. Adsorption characteristics of heavy metal ions onto a low cost biopolymeric sorbent from aqueous solutions. J. Hazard. Mater. 136, 272–280.

Varala, S., Dharanija, B., Satyavathi, B., Rao, V.V.B., Parthasarathy, R., 2016. New

biosorbent based on deoiled karanja seed cake in biosorption studies of Zr(IV): optimization using Box–behnken method in response surface methodology with desirability approach. Chem. Eng. J. 302, 786–800.
Wamba, A.G.N., Lima, E.C., Ndi, S.K., Thue, P.S., Kayem, J.G., Rodembusch, F.S., dos Reis, G.S., de Alencar, W.S., 2017. Synthesis of grafted natural pozzolan with 3-aminopropyltriethoxysilane: preparation, characterization, and application for removal of Brilliant Green 1 and Reactive Black 5 from aqueous solutions. Environ. Sci. Pollut. Res. 24, 21807–21820.
Xia, Y., Yang, T., Zhu, N., Li, D., Chen, Z., Lang, Q., Liu, Z., Jiao, W., 2019. Enhanced adsorption of Pb(II) onto modified hydrochar: modeling and mechanism analysis. Bioresour. Technol. Rep. 288, 121593.
Yang, J., Zhao, Y., Ma, S., Zhu, B., Zhang, J., Zheng, C., 2016. Mercury removal by magnetic biochar derived from simultaneous activation and magnetization of sawdust. Environ. Sci. Technol. 50, 12040–12047.
Yazdani, M.R., Duimovich, N., Tiraferri, A., Laurell, P., Borghei, M., Zimmerman, J.B., Vahala, R., 2019. Tailored mesoporous biochar sorbents from pinecone biomass for the adsorption of natural organic matter from lake water. J.Mol. Liq. 291, 111248.
Yusuf, M., Khan, M.A., Abdullah, E.C., Elfghi, M., Hosomi, M., Terada, A., Riya, S., Ahmad, A., 2016. Dodecyl sulfate chain anchored mesoporous graphene: synthesis and application to sequester heavy metal ions from aqueous phase. Chem. Eng. J. 304, 431–439.
Zhang, Q., Yang, Q., Phanlavong, P., Li, Y., Wang, Z., Jiao, T., Peng, Q., 2017. Highly efficient lead(II) sequestration using size-controllable polydopamine microspheres with superior application capability and rapid capture. ACS Sustain. Chem. Eng. 5 (5), 4161–4170.
Zhou, H., Long, Y., Meng, A., Chen, S., Li, Q., Zhang, Y., 2015. A novel method for kinetics analysis of pyrolysis of hemicellulose, cellulose, and lignin in TGA and macro-TGA. RSC Adv. 5, 26509–26516.
Zhou, N., Chen, H., Xi, J., Yao, D., Zhou, Z., Tian, Y., Lu, X., 2017. Biochars with excellent Pb(II) adsorption property produced from fresh and dehydrated banana peels via hydrothermal carbonization. Bioresour. Technol. Rep. 232, 204–210.